



Dynamics of bond breaking and formation in polyethylene near shock front

Hao Liu ^{1,2,*}, Hao Zhou,^{3,4,*} Wei Kang ^{2,†}, Ping Zhang,^{2,5} Huiling Duan,^{2,3} Weiyang Zhang,^{2,6} and X. T. He^{2,5}

¹Department of Applied Physics, School of Physics and Electronics, Hunan University, Changsha 410082, China

²HEDPS, Center for Applied Physics and Technology, and College of Engineering, Peking University, Beijing 100871, China

³Department of Mechanics and Engineering Science, College of Engineering, Peking University, Beijing 100871, China

⁴Division of Engineering and Applied Science, California Institute of Technology, Pasadena, California 91125, USA

⁵Institute of Applied Physics and Computational Mathematics, Beijing 100088, China

⁶China Academy of Engineering Physics, Mianyang 621900, China



(Received 27 February 2020; accepted 28 July 2020; published 17 August 2020)

In a systematic study of shock wave propagating in crystalline polyethylenes using molecular dynamics method and the electron force field (eFF) potential, we show that microscopic structure of shock front is significantly affected by the anisotropy of long carbon chain and the bond breaking and recombination dynamics. However, macroscopic properties measured in Hugoniot experiments, such as compression ratio and shock velocity, are not sensitive to carbon chain anisotropy and bond dynamics. Our work also display that hydrogen molecules are formed when the piston speed is in the region between 10 km/s and 30 km/s. However, carbon-hydrogen pair distribution function does not display an indication of carbon-hydrogen phase segregation.

DOI: [10.1103/PhysRevE.102.023207](https://doi.org/10.1103/PhysRevE.102.023207)

I. INTRODUCTION

Shock wave has fundamental significance in the fields of inertial confinement fusion (ICF) [1–4], high-energy-density physics (HEDP) [5,6], compressible turbulences [7–9], and astrophysics [10,11], as it is the most practicable and efficient way to generate conditions of extremely high pressure and high temperature. Hydrocarbon materials are widely used as ablating materials of targets in ICF. They were also used to demonstrate phase separation at carbon-rich planetary interior conditions [12,13]. Therefore, propagation of shock waves in hydrocarbons is an important scientific issue, which, however, has not been thoroughly investigated.

In addition to the extreme condition which is far from equilibrium near the shock front [14–16], propagation of shock waves in hydrocarbons is also accompanied by a series of complex processes such as bond breaking, bond recombination, molecule formation, as well as phase transition and phase separation. The various time scale of these processes and the far-from-equilibrium condition make the propagation more intricate, and also more interesting.

Molecular dynamics (MD) simulations have been proved to be a valid way to investigate dynamical processes of shock wave at atomistic scale. The simulations are usually carried out using a variety of force fields or potentials such as embedded-atom method (EAM) potential [17], adaptive intermolecular reactive empirical bond order (AIREBO) [18,19], tight-binding molecular dynamics (TBMD) [20,21], and electron force field (eFF) [22,23]. However, for shock waves generated by strong lasers, which are typical in ICF and relevant experiments, charge transfer and strong ionization of

electrons as well as bond breaking and recombination in the vicinity of the far-from-equilibrium shock front are important features [23]. This makes the eFF method a preferred choice to illustrate nonequilibrium dynamical properties of shock waves propagating in hydrocarbons.

The eFF method is a first-principles-based method proposed by Su and Goddard [22]. It describes electrons using floating spherical Gaussian orbitals and treats nuclei as classical point-charge particles. The expression of Pauli terms in the eFF method plays a crucial role for a relatively accurate description of formation and breaking of valence bonds. Under high temperature and high-energy-density conditions, the eFF method prevents over-expansion of electron wave packets by adding a harmonic constraint, which makes the description of electronic excitation more reasonable under these extreme conditions. With all these features, there are several successful examples of this method in the study of dense plasmas and shock propagations [22–26].

In this work, we present a systematic study of dynamical properties of shock waves propagating in crystal polyethylenes (PE) using the MD method together with the eFF potential. We show that microscopic structure of shock front is significantly affected by the anisotropy of long carbon chain and the bond breaking and recombination dynamics. However, macroscopic properties measured in Hugoniot experiments, such as compression ratio and shock velocity, are not sensitive to carbon chain anisotropy and bond dynamics. Our work also display that hydrogen molecules are formed when the piston speed is in the region between 10 km/s and 30 km/s. However, pair distribution functions of carbon and hydrogen do not display an indication of phase segregation of any kinds.

The rest of this article is organized as follows. Methodology and simulation details are presented in Sec. II. Numerical

*These authors contributed equally to this work.

†weikang@pku.edu.cn

results and discussions are shown in Sec. III. Section IV concludes the entire work with a short summary.

II. METHODOLOGY AND COMPUTATIONAL DETAILS

Propagation of shock waves in PE is simulated using the eFF [22] method implemented in the parallel molecular dynamics code LAMMPS [27]. Nuclei in eFF are modeled as classical point-charge particles, while electrons are represented in the form of electronic wave functions. The wave function of each electron in eFF is approximated as a floating Gaussian wave packet,

$$\Psi(\mathbf{r}) \propto \exp \left\{ -\left[\frac{1}{s^2} - \frac{2p_s}{s} \frac{i}{\hbar} \right] (\mathbf{r} - \mathbf{x})^2 - \frac{i}{\hbar} \mathbf{p}_x \cdot \mathbf{r} \right\}, \quad (1)$$

where s represents the size of wave packets, \mathbf{x} is the center position of the wave packet, and p_s and \mathbf{p}_x are corresponding momentums of s and \mathbf{x} . Substituting Eq. (1) into the time-dependent Schrödinger equation, the evolution equation of electrons can be derived as

$$\begin{aligned} \dot{\mathbf{p}}_x &= -\frac{\partial V}{\partial \mathbf{x}}, & \mathbf{p}_x &= m_e \dot{\mathbf{x}}, \\ \dot{p}_s &= -\frac{\partial V}{\partial s}, & p_s &= \frac{3}{4} m_e \dot{s}, \end{aligned} \quad (2)$$

where $V = V_{ii} + V_{ie} + V_{ee} + E_{KE} + E_{PR}$ is the total energy, V_{ii} , V_{ie} , and V_{ee} are pairwise Coulomb interactions between nuclei and electrons, E_{KE} is the kinetic energy of wave packets, and E_{PR} is the Pauli exclusion energy term of electrons (as fermions.) It is a key ingredient to describe bond formation and breaking in the eFF method.

A zigzag-chain hydrocarbon molecule $C_{12}H_{26}$ is used in the simulation to approximately describe the dynamics of PE following Theofanis *et al.* [26]. Before creating a large-size system to simulate the propagation of shock waves, a small super cell of $C_{12}H_{26}$ was built first and the structure was sufficiently relaxed to equilibrium to minimize artificial stresses. The super cell has a size of $13.86 \text{ \AA}(x) \times 9.44 \text{ \AA}(y) \times 30.84 \text{ \AA}(z)$ and a corresponding density of 0.95 g/cm^3 . It contains two carbon chains consisting of 24 carbon nuclei, 52 hydrogen nuclei and 196 electrons. The carbon chain in the super cell is placed along the z axis, as displayed in Fig. 1(a). Large systems to be shocked are then constructed by replicating the super cell in three dimensions.

Two large systems are constructed from the small cell to illustrate dynamical features arising from different orientations of carbon chains. In one of the system, the shock direction is placed perpendicular to the carbon chain, i.e., along the x axis, and it is labeled as ‘‘lateral shock’’ case hereafter, as displayed in Fig. 1(b). The system has a dimension of $1239.34 \text{ \AA} \times 28.30 \text{ \AA} \times 30.84 \text{ \AA}$, containing $90 \times 3 \times 1$ super cells (73 032 particles.) In the other case, the shock direction is parallel to the carbon chain, i.e., along the z axis, which is called ‘‘longitudinal shock’’ case, as shown in Fig. 1(c). The system contains $2 \times 3 \times 45$ super cells with 73 440 particles. Its dimension is $27.71 \text{ \AA} \times 28.32 \text{ \AA} \times 1382.5 \text{ \AA}$. Since artificial stresses could be introduced during the construction of the large system, a Nose-Hoover thermostat [28] is used to control the temperature of the whole system at 300 K for 1750 fs before the propagation of shocks starts.

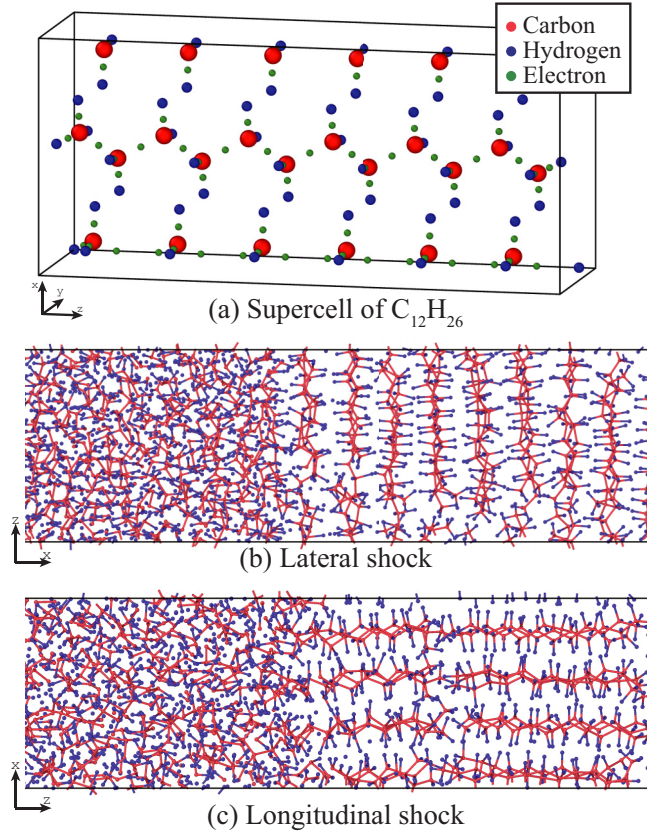


FIG. 1. Schematic illustration of the polyethylene system, where panel (a) is the supercell of $C_{12}H_{26}$ used to construct large systems for the propagation of shockwaves. Red, blue, and green beads represent carbon nuclei, hydrogen nuclei, and electrons, respectively; panels (b) and (c) display the relation of carbon chain’s orientation to the propagation direction of shock waves. Bonds are shown as red lines.

It should be noted that the eFF method consumes significantly more central-processing-unit (CPU) time than a conventional MD calculation. A benchmark from LAMMPS website shows that it is roughly 300 times slower (CPU time per time step per particle) than a conventional Lennard-Jones potential, as it takes electrons’ motion into consideration [29]. A time step on the order of an attosecond is required to capture the continuous trajectory of electrons, when the true electronic mass is used in the simulation. To take a larger time step in the simulations and save computing resources, the electron mass was set as 1 amu rather than the true electron mass of 0.00055 amu in previous works [30]. This choice is fine for equilibrium systems since electron mass has minor effect on ‘‘static’’ properties of the system, such as chemical structures and thermal quantities. However, the choice of electron mass has a significant influence on the ‘‘dynamic’’ aspects of the system because the relaxation time is directly related to electron mass. To investigate the influence of electron mass, testing simulations with $m_e = 0.01$ amu and $m_e = 0.00055$ amu are performed. Results show that a larger electron mass leads to a faster shock wave and accelerates the bond breaking and recombination processes. Therefore, the true electron mass of 0.00055 amu is used in all the simulations, even though a high

computational cost is incurred. The time step in simulations is set to be 0.2 attosecond accordingly.

Reflecting boundaries are used at the right end of the simulation box along the shock direction. The boundaries act as “momentum mirrors” for those particles crossing the boundary in one time step. A reflecting wall moving at a constant speed v_p is used as a piston to drive the shock wave from left to right, which is similar to those used in previous works [23,31]. The v_p explored in this work is 2.5 km/s, 5 km/s, 10 km/s, 15 km/s, 20 km/s, and 30 km/s. Along other two directions periodic boundaries are employed.

To illustrate nonequilibrium dynamical effects in the vicinity of the shock front, the simulation box is divided into a series of slices along the shock direction to get the statistics of various quantities. The thickness of each slice is 1.59 Å, i.e., 3.0 Bohr. Thermodynamical quantities such as density, temperature, and pressure in each slice are calculated as statistical averages [32]. Note that, since electrons in the eFF method is considered as wave packets, there is an extra degree of freedom for the size s of the wave packet, in addition to their three translational degrees of freedom. Therefore, the electronic temperature T_e in eFF is calculated as [30]

$$T_e = \frac{1}{4N_e k_B} \sum_i^{N_e} m_e \left(\mathbf{v}_{\mathbf{x},i}^2 + \frac{3}{4} v_{s,i}^2 \right), \quad (3)$$

where N_e is the number of electrons in a slice, k_B is the Boltzmann constant, $\mathbf{v}_{\mathbf{x},i}$ is the translational velocity of the i th particle, and $v_{s,i}$ is the variation rate of the wave-packet size.

III. RESULTS AND DISCUSSIONS

A. Thickness of the shock front

It is generally difficult to detect fine structures of dynamical processes near a shock front in experiments, since the shock front is usually confined in a thin layer and physical properties change sharply across the shock front. The thickness δ of a shock front is one of the few physical quantities that might be experimentally measured. From theoretical point of views, the definition of δ is not unique, since several physical quantities, such as density, temperature, and velocity, have a sharp jump across the shock front. Each of them can be used to define a δ . As displayed in the subplot of Fig. 2(a), we use the scale length of density variation as the definition of δ [33], since optical reflectivity method is the most common way to measure δ in experiments [34–37]. It is based on detecting the change of electronic number densities near the shock front. Other ways to define δ are also possible. These various definitions might give different δ magnitudes, but they in general should be on the same order of magnitude.

Figure 2 shows the density profile along the shock direction for various v_p , where (a) is for lateral shocks and (b) is for longitudinal shocks. The thickness δ of the shock front can then be measured from the profiles, as listed in Table I. Also listed in the table are shock velocities v_s , which are calculated as the distance traveled by the shock front divided by the traveling time. Compression ratios η of the shock wave can be obtained through the density continuity as $\eta = v_s / (v_s - v_p)$. It is noticed that, in addition to the sharp density change at the shock front, a small increase in density can also be

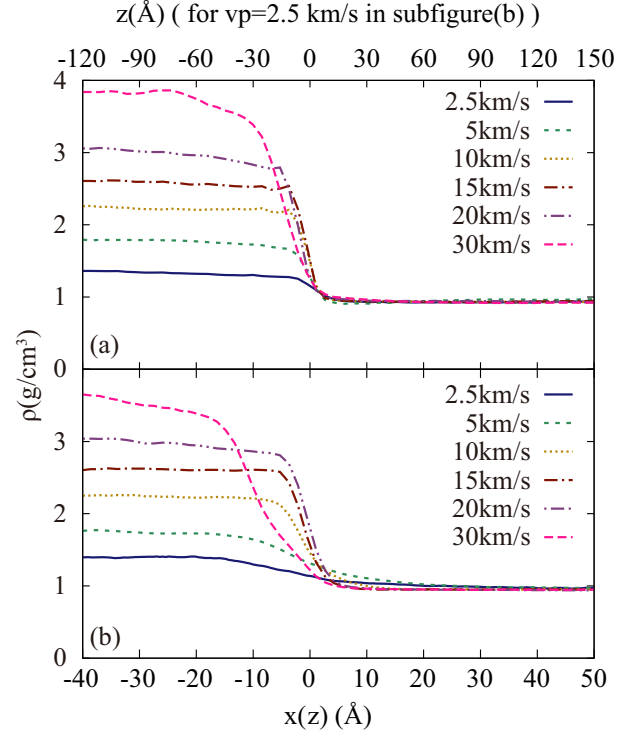


FIG. 2. Density ρ variations along the shock direction at selected v_p , where panels (a) and (b) correspond to lateral and longitudinal shocks, respectively. Note that in panel (b) the scale of the z axis for $v_p = 2.5$ km/s is displayed on the top of the figure.

observed behind the shock front of strong shocks, i.e., shocks with $v_p \geq 20$ km/s. This is an indication of some slow relaxation processes behind the shock front, which will be further discussed in the following sections. This slow increase also causes uncertainties if one measures η as the density ratio at both ends of the abscissa in Fig. 2.

For both lateral and longitudinal shocks, η and v_s are roughly the same for a given v_p . This shows that the orientation of carbon chains does not affect the macroscopic propagation speed and compression of shock waves. This phenomenon should be quite general, although it is observed through our model PE systems, since the orientation of carbon chains does not change the number and type of chemical

TABLE I. Compression ratio η , thickness of shock front δ , and speed of shockwave v_s under lateral and longitudinal shocks at selected piston speed v_p .

v_p (km/s)	Lateral shock			Longitudinal shock		
	η	δ (Å)	v_s (km/s)	η	δ (Å)	v_s (km/s)
2.5	1.43	9.0	8.31	1.48	71.4	7.71
5	1.89	5.3	10.62	1.85	23.8	10.88
10	2.34	5.3	17.46	2.37	10.6	17.30
15	2.75	4.2	23.57	2.77	6.9	23.47
20	3.18	5.3	29.17	3.15	6.9	29.30
30	4.01	10.1	39.97	3.79	16.4	40.75

bonds. After the sweep of the shock, the final energetic and thermal states should be roughly the same when all chemical and physical processes are completed.

However, microscopic fine structures of shock fronts are strongly affected by the local structure. For example, with the increase of v_p , δ first decreases to a minimum and then increases for both lateral and longitudinal shocks. This behavior of δ can be qualitatively understood by Landau's theory of shock front thickness [38], which pointed out that $\delta \propto \Delta p^{-1}$ for weak shock waves and $\delta \propto l$ for strong shock waves. Here, Δp is the pressure difference across the shock front, and l is an average mean free path in the vicinity of the shock front. In a coordinate system moving with the shock front, l of a strong shock wave basically represents the penetrating depth relating to high temperature materials after the shock front penetrating into low temperature materials before the shock front. A theoretical model of l further shows that $l \propto M$, the Mach number [39]. So, for weak shock waves, where v_p is relatively low, δ is controlled by the compression effect of shock waves, which reduces δ . While for strong shock waves, where the compression effect is limited to $\eta \sim 4$, δ is then determined by the thermal heating of shock waves, which makes δ increase with v_p .

Figure 2 also shows that δ under longitudinal shock is about 8 times larger than that under lateral shock at $v_p = 2.5$ km/s, which is attributed to the anisotropic distribution of C-C bonds. At a low piston speed of $v_p = 2.5$ km/s, the structure of a carbon chain is not destroyed yet. Interaction between carbon atoms along the carbon chain is much stronger than those interactions on other directions, which means that it is much easier to compress the PE at places where no C-C bonds are presented, and the increasing of density near the shock front is mainly provided by the compression between chains. The characteristic scale of density change is then much larger under longitudinal shocks than that under lateral shocks.

B. Distribution of thermodynamical quantities

In addition to the behavior of δ , thermodynamical quantities in the vicinity of the shock front are also strongly affected by the anisotropy of carbon chains, especially for weak shock waves. Figure 3 shows the profile of pressure components near the shock front at $v_p = 2.5$ km/s, where P_{zz} is the pressure component along the carbon chain. It shows that P_{zz} is significantly smaller than other components behind the

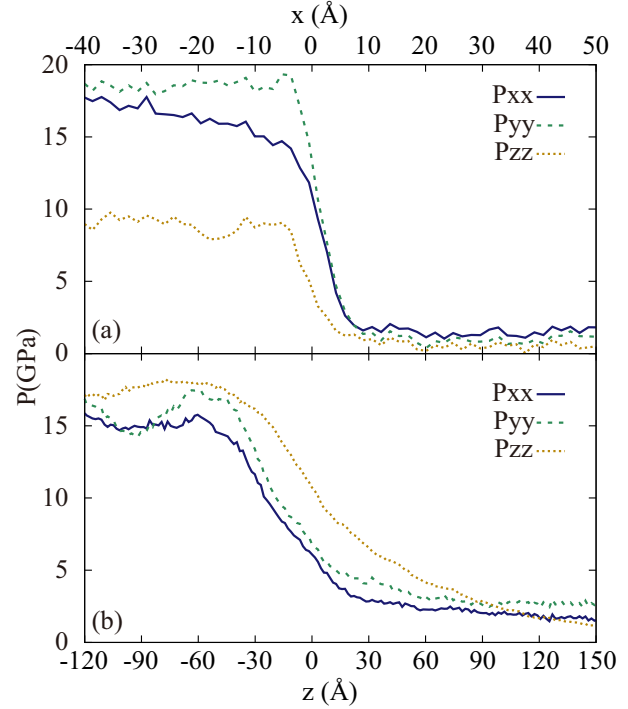


FIG. 3. Profiles of pressure components along the shock direction under lateral (a) and longitudinal (b) shock at $v_p = 2.5$ km/s. P_{zz} is the pressure component along the carbon chain.

shock front for the lateral shock, while the profiles of pressure components are nearly the same for the longitudinal shock.

Pressure components behind the shock front at different v_p are listed in Table II. Also listed are degrees of pressure anisotropy α , defined as $\alpha = 2P_{zz}/(P_{xx} + P_{yy})$, with P_{zz} along the direction of the carbon chain. Table II shows that the degree of anisotropy is attenuated with increasing v_p , resulted from the dissociation of carbon chains. The chain structure is nearly undamaged at $v_p = 2.5$ km/s, as we shall show in the next subsection. So the degree of anisotropy for pressure components is the largest. With the increasing of v_p , the carbon chain gradually breaks into smaller pieces, making the system more isotropic.

However, anisotropy effect on the overall propagation of shock waves is not significant. Table I shows that even at $v_p = 2.5$ km/s, compression ratio η and shock velocity v_s

TABLE II. The value of pressure components behind the shock front for lateral and longitudinal shock. P_{xx} , P_{yy} , and P_{zz} correspond to diagonal element of pressure tensor; P_{zz} is the pressure component along the direction of carbon chain. $\alpha = 2P_{zz}/(P_{xx} + P_{yy})$ is a parameter measuring the degree of pressure anisotropy.

v_p (km/s)	Lateral shock				Longitudinal shock			
	P_{xx} (GPa)	P_{yy} (GPa)	P_{zz} (GPa)	α	P_{xx} (GPa)	P_{yy} (GPa)	P_{zz} (GPa)	α
2.5	17	19	9	0.5	15	16	18	1.16
5	45	47	35	0.76	45	45	48	1.07
10	140	145	110	0.77	147	147	14	1.00
15	270	270	240	0.89	275	275	275	1.00
20	420	420	420	1.00	425	425	425	1.00
30	880	880	880	1.00	820	820	820	1.00

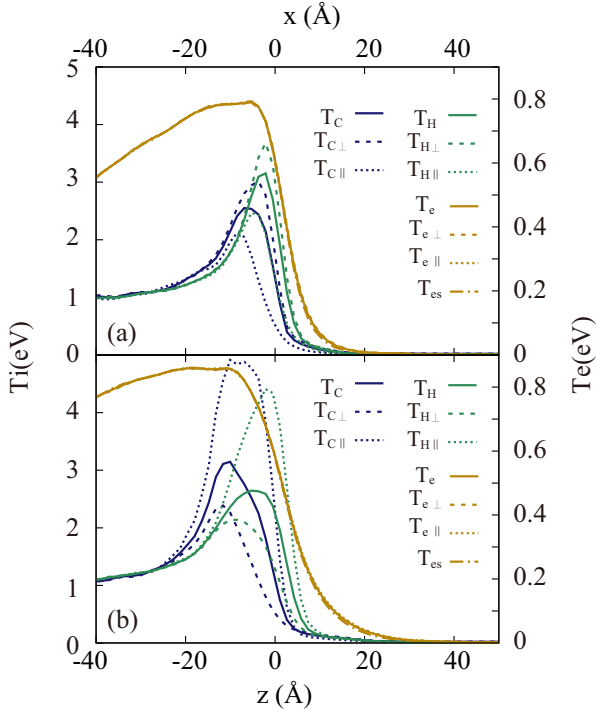


FIG. 4. Profiles of temperature components along the shock direction under lateral (a) and longitudinal (b) shock at $v_p = 30$ km/s. The subscripts C, H, and e correspond to the temperature components of carbon nuclei, hydrogen nuclei, and electrons, respectively, and the subscripts \perp and \parallel correspond to the temperature components perpendicular and parallel to the shock direction, respectively. The s in the subscript represents the temperature component associated with the size of electronic wave packets.

are quite similar at the same v_p no matter the PE system is under lateral or longitudinal shock. This implies that Hugoniot measurements, which usually measure v_s , may be difficult to demonstrate the anisotropic effect caused by the orientation of carbon chains in the sample.

Temperature profiles carry the information of energetic relaxation and chemical reactions near the shock front. Since the system is composed of much more particle species than those in a deuterium system, temperature profiles afford more microscopic features. For shocks driven by high v_p , the feature of temperature profiles is quite similar to what we observed in deuterium system [23] with the same simulation technique. Figure 4 shows the temperature profiles at $v_p = 30$ km/s as an example. It shows that all temperature components of carbon and hydrogen have a high “overshoot” peak at the shock front. Similar to shocks in deuterium simulated using the eFF method, this feature is caused by the combination of kinetic energy relaxation and fast bond breaking processes.

Figure 4 also shows that electronic temperature components perpendicular and parallel to the propagation direction of shock do not separate as ions do, and they are always smaller than the ionic temperature in the downstream region. This agrees with the previous findings in deuterium [23] simulated using the eFF method, and suggests that distinguishing ionic temperature and electronic temperature in the hydrodynamical modeling of the ICF implosion process is

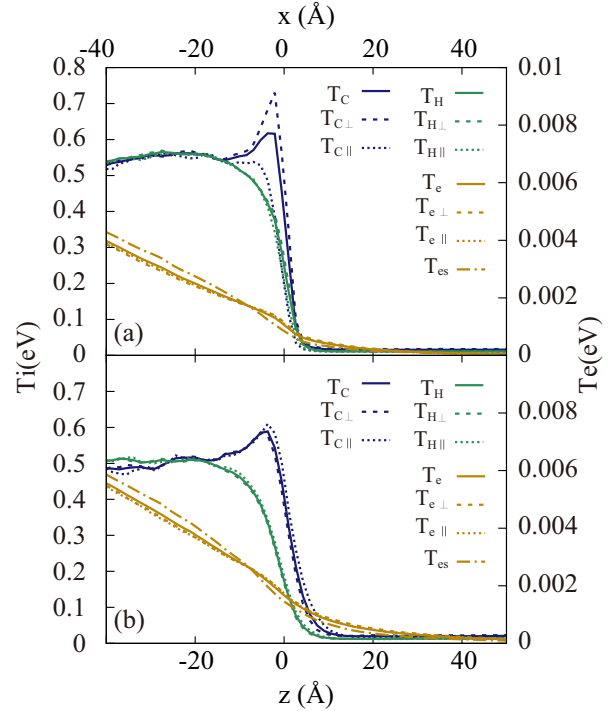


FIG. 5. Profiles of temperature components along the shock direction under lateral (a) and longitudinal (b) shock at $v_p = 10$ km/s. The meaning of subscripts is the same as that in Fig. 4.

necessary. Note that, equilibrium between electrons and ions is not reached in our simulations due to limit length of the PE system. The T_e therefore does not equal to the ionic temperature on the left side of the figures.

Temperature profiles at $v_p = 10$ km/s are displayed in Fig. 5. Its feature is typical for weak shocks propagating in PE. It is noticed that an important characteristic of the temperature profile is that the parallel and perpendicular temperature components of hydrogen do not separate as those under strong shocks. Instead, the two components are close to each other, suggesting that there is no relaxation of kinetic energy among different directions. As we shall show in the next subsection, at $v_p = 10$ km/s, the C-C bonds and C-H bonds are broken. So, this feature actually implies that energy delivered by the shock wave is first used to break bonds.

C. Structures of carbon chain

An important advantage of the eFF method in the study shock waves is that bond formation and breaking processes can be captured based on dynamical behaviors of electrons, rather than based on prescribed bonding formation conditions in conventional classical MD simulations. Radial distribution functions (RDF) are used to reveal the change of microscopic structures in the hydrocarbon material. We calculate the RDF following

$$g_{\alpha\beta}(r) = \frac{V}{N^2} \left\langle \sum_{i(\alpha)} \sum_{j(\beta)} \delta(r - r_{ij}) \right\rangle, \quad (4)$$

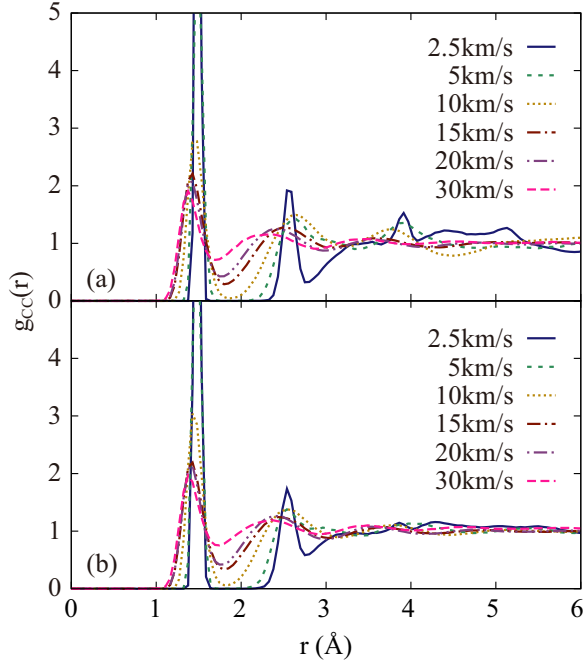


FIG. 6. Profiles of C-C RDF behind the shock front under lateral (a) and longitudinal (b) shock at selected v_p .

where V is the volume of interest, N is the particle number in the volume, and $i(\alpha)$ and $j(\beta)$ are particle indexes of type α and β , respectively.

$g_{CC}(r)$'s, namely, RDFs of carbon-carbon, far behind the shock front (downstream) are given in Fig. 6, where Fig. 6(a) is for lateral shocks and Fig. 6(b) is for longitudinal shocks. The first peak at $r = 1.53$ Å corresponds to the C-C bonds in hydrocarbon chains. The height of the peak decreases with the increase of v_p , indicating that more C-C bonds are broken at increasing v_p . In addition, there are two peaks at $r \approx 2.65$ Å and 3.97 Å at low v_p , corresponding to the second and the third nearest carbon atoms along the carbon chain. With the increase of v_p , these peaks gradually disappear, showing that the hydrocarbon system transforms from crystalline to liquid or gas states as v_p increases. Comparing g_{CC} under lateral shock with that under longitudinal shock, Fig. 6 shows that g_{CC} has more peak structures at larger r for lateral shock at $v_p < 15$ km/s. This suggests that lateral shock at low v_p causes less deformation or breaking of carbon chains.

$g_{CH}(r)$'s (RDFs of carbon-hydrogen) are displayed in Fig. 7. The first peak at $r = 1.11$ Å corresponds to the C-H bonds in the carbon chain. The trend of C-H bond breaking is similar to that of C-C bonds. However, the difference of g_{CH} between lateral shock and longitudinal shock is less significant. This is because C-H bonds are much weaker than C-C bonds. They are much easier to leave their equilibrium places due to heating effect of the shock.

Recently, phase separation of carbon and hydrogen in hydrocarbon materials has attracted much attention [13,40,41]. It is considered as a necessary premise for the formation of diamonds. If such phase separation happened, there would be a plateau appearing on the right side of the g_{CH} curve. Otherwise, g_{CH} would approach 1 at large r in a homogeneous

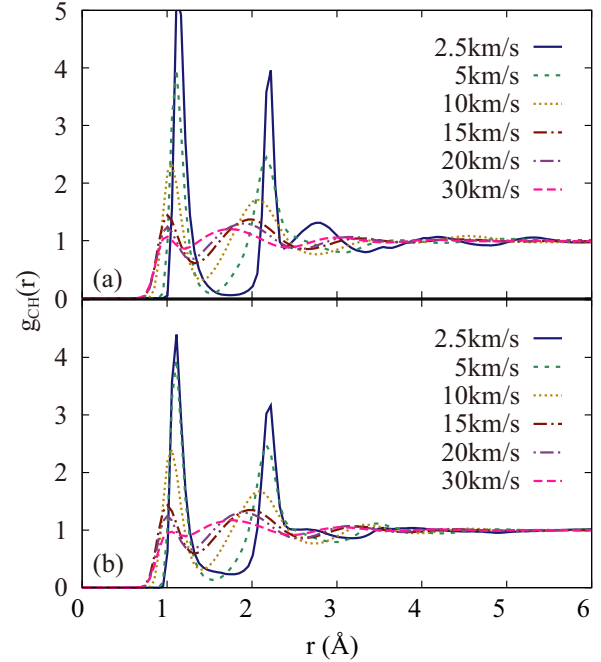


FIG. 7. Profiles of C-H RDF behind the shock front under lateral (a) and longitudinal (b) shock at selected v_p .

system. Figure 7 shows that g_{CH} is roughly equal to 1, and no plateau is observed for $v_p > 10$ km/s, when the system is melted. These results are partially in agreement with experiments on polyethylene [41], in which no phase separation was observed.

Since RDF can only qualitatively illustrate the formation and breaking of bonds, it is necessary to use the number distribution of hydrocarbon chains of various lengths to quantitatively describe the effect of shock waves on bond formation and breaking. The bonding criteria used in this work are as follows. For any two carbon nuclei at a distance r , there is a C-C bond between them if $L_{CC} - \delta L_{CC} \leq r \leq L_{CC} + \delta L_{CC}$, and simultaneously there are two bonding electrons of different spins inside the sphere centered at the middle of the two nuclei with the radius $\delta r_{CC} = 0.16$ Å. Here, $L_{CC} = 1.58$ Å is the length of a C-C bond, $\delta L_{CC} = 0.16$ Å is the possible length variation of a C-C bond. The bonding criteria for H-H bond was defined in a similar way with $L_{HH} = 0.74$ Å, $\delta L_{HH} = 0.11$ Å and $\delta r_{HH} = 0.11$ Å. The criteria for C-H bond are slightly different from those of C-C and H-H bonds since carbon has 4 valence electrons while hydrogen has only 1 valence electron. The bonding electron pair is then located at a distance from hydrogen four times of the distance from carbon to approximately maintain the force balance. The parameters for C-H bond are chosen as $L_{CH} = 1.07$ Å, $\delta L_{CH} = 0.16$ Å and $\delta r_{CH} = 0.16$ Å. We use bond number per unit mass instead of bond number density per unit volume to describe the ratio of bond breaking considering the particle number density varies greatly on the two sides of shock front.

Figure 8 displays the distribution of C-C bond number n_{CC} per unit mass along the shock direction. It shows that there is almost no C-C bond breaks at $v_p = 2.5$ km/s. With the increase of v_p , n_{CC} behind the shock front start to decreasing.

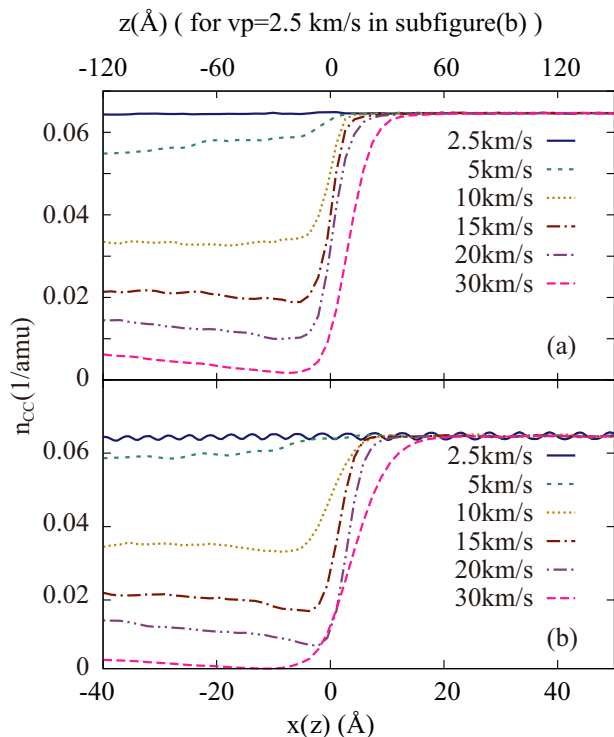


FIG. 8. Profiles of C-C bond number per unit mass under lateral (a) and longitudinal (b) shock at selected v_p . Note that in panel (b) the scale of the z axis for $v_p = 2.5$ km/s is displayed on the top of the figure.

About half of the C-C bonds break after the shock front at $v_p = 10$ km/s and the breaking ratio goes beyond 90% at $v_p = 30$ km/s. It is also noticed that, when the shock is strong enough, i.e., $v_p > 10$ km/s, n_{CC} has a minimum near the shock front and gradually increases with its position moving away from the front, suggesting that some C-C bonds are reconnected after they break near the shock front. This phenomenon is considered as a result of temperature “overshooting” at the shock front [23,31,42], i.e., the effective temperature near the shock front is much higher than that far behind the shock front as a strong nonequilibrium feature near the shock front. The breaking ratio increases following the increasing of effective temperature. In addition, the distribution of n_{CC} under lateral and longitudinal shock is similar at the same v_p , indicating that the orientation of carbon chain has minor effects on the breaking of C-C bonds.

Figure 9 displays the distribution of C-H bond number n_{CH} per amu along the shock direction. Note that for $v_p = 2.5$ km/s in Fig. 9(b), the z axis is displayed on the top of the figure. The behavior of n_{CH} is similar to that of n_{CC} except at very low $v_p = 2.5$ km/s. The n_{CC} profiles in Fig. 8 show that the C-C bonds do not break at this low v_p , suggesting that the frame of the hydro-carbon material is not destroyed. However, the n_{CH} profile in Fig. 9 displays that C-H bonds dissociate slowly after the shock passing the material.

In our simulations, there is only one type of molecule $C_{12}H_{26}$ before the shock. However, after the shock the length of carbon chains varies with the breaking and reconnection of C-C bonds, and exhibits a complicate distribution as a

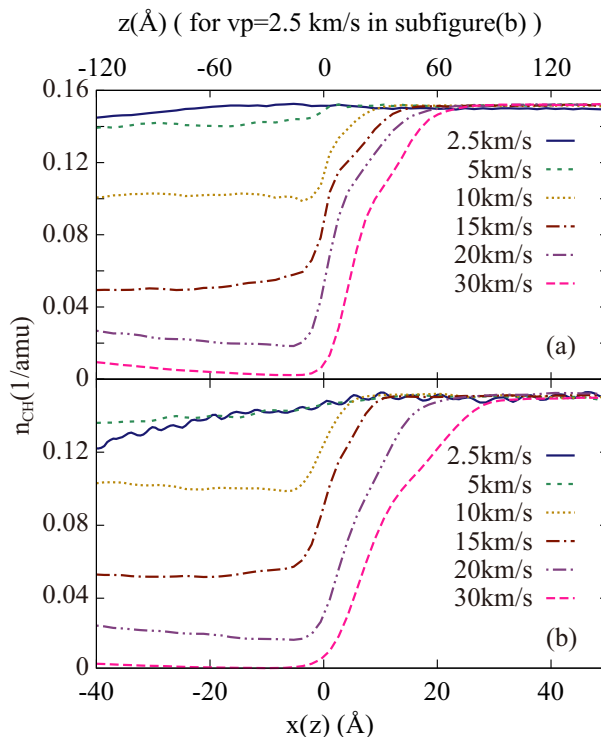


FIG. 9. Profiles of C-H bond number per unit mass under lateral (a) and longitudinal (b) shock at selected v_p . Note that in (b) the scale of the z axis for $v_p = 2.5$ km/s is displayed on the top of the figure.

function of v_p . To calculate the number distribution of hydro-carbon molecules of various length, a connection matrix [43] including all carbon atoms is calculated based on the C-C bond formation criteria. The matrix element is 1 when there is a C-C bond between two carbon atoms, otherwise the matrix element is zero. Then all the carbon chains of a given length are determined using the depth-first traversal searching algorithm [43].

The length distribution of carbon chains behind the shock front are displayed in Fig. 10. Here, the length of carbon chains l_c is defined as the number of carbon atoms it contains. Initially in the sample, l_c of all carbon chains is 12. Figure 10 shows that at $v_p = 2.5$ km/s, very small number of carbon chains with $l_c = 12$ are broken. However, when v_p increases to 10 km/s, almost all the long chains with $l_c = 12$ are broken. The distribution of l_c displays an exponential-law distribution at $v_p \geq 10$ km/s, as illustrated in Fig. 11. Note that the vertical axis is plotted in log scale. The exponential-law distribution is displayed as a straight line in the figure.

The exponential-law distribution of l_c strongly implies that C-C bond connection behind the shock front is completely random, as it is a natural consequence of the following random connection model. Suppose the connection between two adjacent carbon atoms is completely random, and the probability to form a C-C bond is p . Then the probability to find $l_c = 2$ is just p , the probability of two C-C bonds formed among 3 carbon atoms is p^2 , and the probability to form a carbon chain of length l_c is p^{l_c-1} . If this simple picture holds, it also suggests that the hydro-carbon system is completely melted at $v_p \geq 10$ km/s.

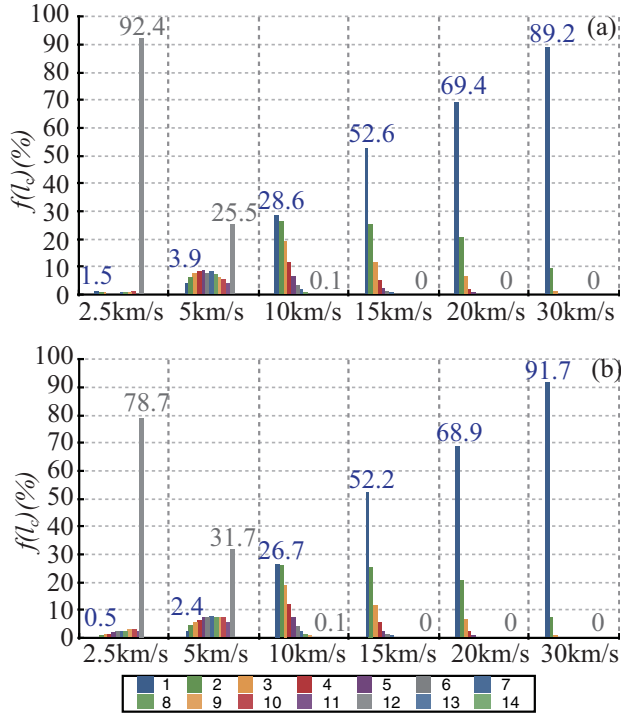


FIG. 10. Length distribution of carbon chains behind the shock front at selected v_p under lateral (a) and longitudinal (b) shock. The length of carbon chains is represented by numbers of carbons in the chain and displayed in different colors.

D. Formation of H₂ molecules

RDFs of H-H behind the shock front are displayed in Fig. 12. Unlike RDFs of C-C and C-H, there is no peak of

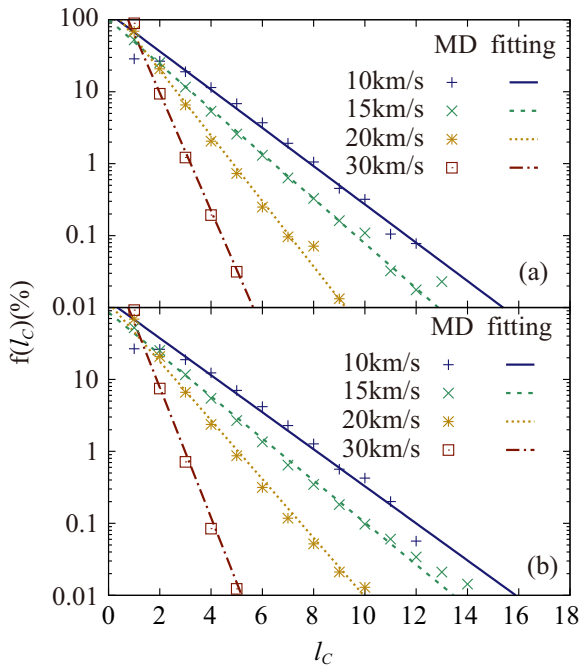


FIG. 11. Exponential law in the length distribution of carbon chains behind the shock front at various v_p under lateral (a) and longitudinal (b) shock. Lines are exponential fittings to the distribution.

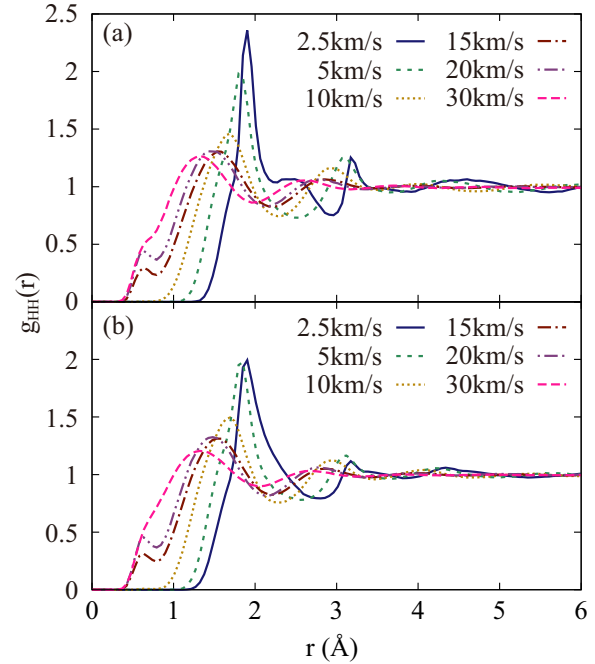


FIG. 12. Profiles of H-H RDF behind the shock wave front under lateral (a) and longitudinal (b) shock at selected v_p .

H-H bond, i.e., peak at $r \approx 0.74 \text{ \AA}$, at relatively slow v_p . Initially, there is no H-H bonds in the molecule of $C_{12}H_{26}$. However, there might be small amount of hydrogen atoms or ions existing in the the system, as displayed in Fig. 9, which shows that some C-H bonds are broken at low v_p . The first peak at $r \approx 2.01 \text{ \AA}$ corresponds to the two hydrogen atoms bonded on the same carbon atom. With the increase of v_p , it is observed that a small peak appears at $r \approx 0.74 \text{ \AA}$ at $v_p = 10 \text{ km/s}$ and 15 km/s , indicating the formation of H₂ molecules under the shock. Further increasing the v_p to 30 km/s , the H-H bond peak disappears, suggesting that H₂ molecules are dissociated into hydrogen atoms or ions.

The formation of H₂ was also noticed by Theofanis *et al.* [26] in their static simulations of PE using the same method. However, the peaks in our dynamical simulation are much more significant than those in their static simulations, which may be caused by the size effect of simulations. Usually, thermal fluctuations in a small-size simulation prevent the formation of bonds and atom clusters.

To capture the dynamical behavior of H₂ formation under shocks, the distribution of H-H bonds number n_{HH} per unit mass along the shock direction are calculated, as shown in Fig. 13. For the shock at $v_p = 10 \text{ km/s}$, which has a very small H-H bond peak in the RDF of H-H behind the shock front (in Fig. 12), Fig. 13 shows that a small number of H-H bonds formed far behind the shock front. That is to say, the generation of hydrogen molecules is much delayed comparing to the arriving of the shock front. This is the result of slow formation speed of H₂ molecules at relatively low temperature.

The number of H-H bonds per unit mass behind the shock front reaches its maximum at $v_p = 20 \text{ km/s}$. There is no delay observed in the formation of H-H bonds with respect to the

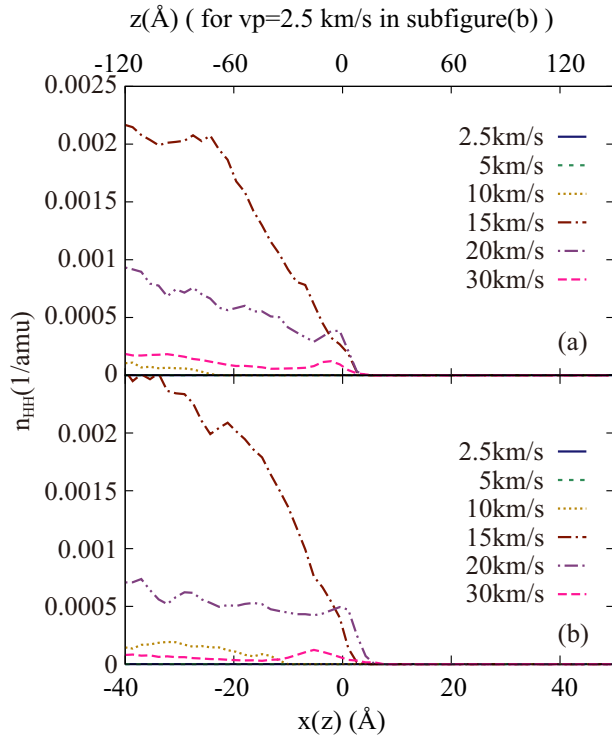


FIG. 13. H-H bond number distribution per unit mass under lateral (a) and longitudinal (b) shock at selected v_p . Note that in (b) the scale of the z axis for $v_p = 2.5$ km/s is displayed on the top of the figure.

arriving of shock, because the forming speed of the H-H bond is accelerated by the relatively high temperature behind the shock.

When v_p is further increased, the temperature behind the shock front is too high and some H-H bonds start to dissociate. As a result, the amount of H-H bonds decrease when v_p increases.

E. Charge separation

Figure 14 displays the net charge density along the shock direction at various v_p . At small v_p , no charge separation is observed, suggesting that electrons are tightly bonded around C and H atoms, and ionization is negligible. When v_p is greater than 10 km/s, charge separation emerges. However, it does not form a dipole layer centered at the shock front, as predicted by the traditional theory of shock waves. Instead, positive charge is distributed in all downstream region behind the shock front, which is similar to what we observed in deuterium system [23] using the same method and is attributed to the lacking of negative charge supplies in the downstream region. Before the shock front, negative charge is concentrated in a finite length scale l_e , which increases with v_p . It is noticed that the length scale of negative charge distribution is much more localized than that in the deuterium system [23] simulated with the same method, where negative charge is found far before the shock front. This difference mainly comes from the carbon ions, each of which carries four positive charges so that it affords stronger attraction to electrons.

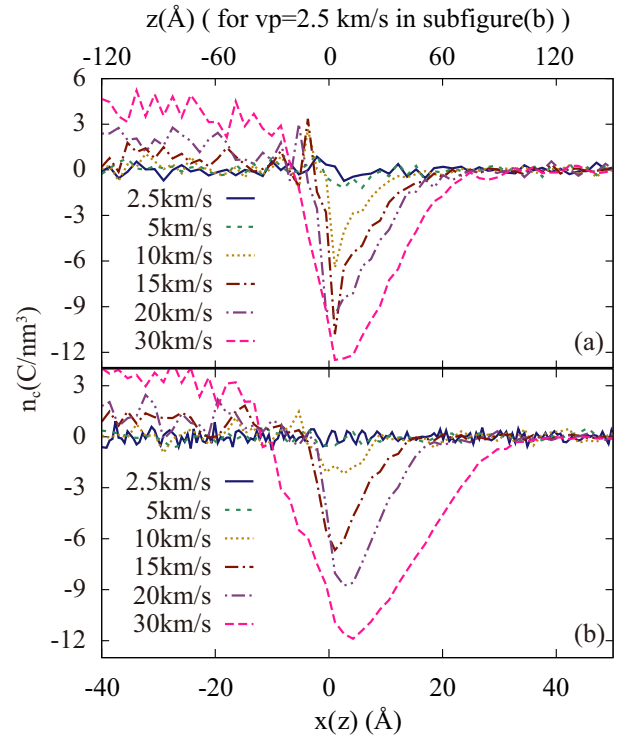


FIG. 14. Profiles of charge density under lateral (a) and longitudinal (b) shock at different v_p . Note that in (b) the scale of the z axis for $v_p = 2.5$ km/s is displayed on the top of the figure.

IV. SUMMARY

In summary, we have presented a systematic investigation of shock waves propagating in crystalline PE. The dynamical structure of shock wave front, including shock front thickness, nonequilibrium distribution of thermodynamical quantities, dynamical processes of bond formation and breaking, and charge separation are discussed in detail. Although the formation of H₂ molecules is observed in the simulation, however, we do not find there is an indication of carbon-hydrogen phase separation. These results may help to understand how shock waves propagate in the ablative layer of a ICF fuel parcel. They may also provide some hints to recent shock experiments in hydrocarbon materials. We note that one should be cautious that these results are what one gets using the eFF method, in which several major approximations have been made. The final picture may be arrived at in the future with the advance of first-principles quantum-mechanical description to the dynamics of electrons.

ACKNOWLEDGMENTS

This work is financially supported by the National Key Research and Development Program of China under Grant No. 2017YFA0403200, NSFC (Grant No. 11805061), Natural Science Foundation of Hunan Province, China (Grant No. 2019JJ50072), the Science Challenging Project under Grant No. TZ2016001, and the Fundamental Research Funds for the Central Universities.

- [1] R. Betti, C. D. Zhou, K. S. Anderson, J. L. Perkins, W. Theobald, and A. A. Solodov, *Phys. Rev. Lett.* **98**, 155001 (2007).
- [2] X. T. He, J. W. Li, Z. F. Fan, L. F. Wang, J. Liu, K. Lan, J. F. Wu, and W. H. Ye, *Phys. Plasmas* **23**, 082706 (2016).
- [3] Z. Fan, Y. Liu, B. Liu, C. Yu, K. Lan, and J. Liu, *Matter Radiat. Extremes* **2**, 3 (2017).
- [4] E. Campbell, V. Goncharov, T. Sangster, S. Regan, P. Radha, R. Betti, J. Myatt, D. Froula, M. Rosenberg, I. Igumenshchev, W. Seka, A. Solodov, A. Maximov, J. Marozas, T. Collins, D. Turnbull, F. Marshall, A. Shvydky, J. Knauer, R. McCrory, A. Sefkow, M. Hohenberger, P. Michel, T. Chapman, L. Masse, C. Goyon, S. Ross, J. Bates, M. Karasik, J. Oh, J. Weaver, A. Schmitt, K. Obenschain, S. Obenschain, S. Reyes, and B. V. Wonterghem, *Matter Radiat. Extremes* **2**, 37 (2017).
- [5] R. P. Drake, *High-Energy-Density Physics: Fundamentals, Inertial Fusion, and Experimental Astrophysics* (Springer Science & Business Media, Berlin, 2006).
- [6] B. Y. Sharkov, D. H. Hoffmann, A. A. Golubev, and Y. Zhao, *Matter Radiat. Extremes* **1**, 28 (2016).
- [7] J. Wang, Y. Shi, L.-P. Wang, Z. Xiao, X. He, and S. Chen, *Phys. Fluids* **23**, 125103 (2011).
- [8] J. Wang, Y. Shi, L.-P. Wang, Z. Xiao, X. He, and S. Chen, *J. Fluid Mech.* **713**, 588 (2012).
- [9] J. Wang, Y. Shi, L.-P. Wang, Z. Xiao, X. T. He, and S. Chen, *Phys. Rev. Lett.* **108**, 214505 (2012).
- [10] A. R. Bell, *Mon. Not. R. Astron. Soc.* **182**, 147 (1978).
- [11] J. F. Hansen, M. J. Edwards, D. Froula, G. Gregori, A. Edens, and T. Ditmire, in *High Energy Density Laboratory Astrophysics* (Springer, Berlin, 2005), pp. 61–67.
- [12] M. Ross, *Nature* **292**, 435 (1981).
- [13] D. Kraus, J. Vorberger, A. Pak, N. Hartley, L. Fletcher, S. Frydrych, E. Galtier, E. Gamboa, D. Gericke, S. Glenzer *et al.*, *Nat. Astron.* **1**, 606 (2017).
- [14] Y. Gan, A. Xu, G. Zhang, X. Yu, and Y. Li, *Physica A* **387**, 1721 (2008).
- [15] C. Lin, A. Xu, G. Zhang, and Y. Li, *Combust. Flame* **164**, 137 (2016).
- [16] Y. Gan, A. Xu, G. Zhang, Y. Zhang, and S. Succi, *Phys. Rev. E* **97**, 053312 (2018).
- [17] K. Kadau, T. C. Germann, P. S. Lomdahl, and B. L. Holian, *Science* **296**, 1681 (2002).
- [18] M. Elert, S. Zybin, and C. White, *J. Chem. Phys.* **118**, 9795 (2003).
- [19] T. C. O'Connor, J. Andzelm, and M. O. Robbins, *J. Chem. Phys.* **142**, 024903 (2015).
- [20] S. Bickham, J. Kress, and L. Collins, *J. Chem. Phys.* **112**, 9695 (2000).
- [21] J. D. Kress, S. R. Bickham, L. A. Collins, B. L. Holian, and S. Goedecker, *Phys. Rev. Lett.* **83**, 3896 (1999).
- [22] J. T. Su and W. A. Goddard III, *Phys. Rev. Lett.* **99**, 185003 (2007).
- [23] H. Liu, Y. Zhang, W. Kang, P. Zhang, H. Duan, and X. T. He, *Phys. Rev. E* **95**, 023201 (2017).
- [24] H. Kim, J. T. Su, and W. A. Goddard, *Proc. Natl. Acad. Sci. USA* **108**, 15101 (2011).
- [25] A. Jaramillo-Botero, J. Su, A. Qi, and W. A. Goddard, *J. Comput. Chem.* **32**, 497 (2011).
- [26] P. L. Theofanis, A. Jaramillo-Botero, W. A. Goddard III, T. R. Mattsson, and A. P. Thompson, *Phys. Rev. B* **85**, 094109 (2012).
- [27] S. Plimpton, *J. Comput. Phys.* **117**, 1 (1995).
- [28] S. Nosé, *J. Chem. Phys.* **81**, 511 (1984).
- [29] S. J. Plimpton, Lammmps benchmarks, <http://lammmps.sandia.gov/bench.html>.
- [30] J. T. Su, An Electron Force Field for Simulating Large Scale Excited Electron Dynamics, Ph.D. thesis, California Institute of Technology, 2007.
- [31] H. Liu, W. Kang, Q. Zhang, Y. Zhang, H. Duan, and X. T. He, *Front. Phys.* **11**, 115206 (2016).
- [32] J. H. Irving and J. G. Kirkwood, *J. Chem. Phys.* **18**, 817 (1950).
- [33] L. H. Thomas, *J. Chem. Phys.* **12**, 449 (1944).
- [34] G. R. Cowan and D. F. Hornig, *J. Chem. Phys.* **18**, 1008 (1950).
- [35] E. F. Greene, G. R. Cowan, and D. F. Hornig, *J. Chem. Phys.* **19**, 427 (1951).
- [36] M. Linzer and D. F. Hornig, *Phys. Fluids* **6**, 1661 (1963).
- [37] P. Harris and H. N. Presles, *J. Chem. Phys.* **74**, 6864 (1981).
- [38] L. D. Landau and E. M. Lifshitz, *Course of Theoretical Physics* (Elsevier, Amsterdam, 2013).
- [39] C. Muckenfuss, *Phys. Fluids* **5**, 1325 (1962).
- [40] S. S. Lobanov, P.-N. Chen, X.-J. Chen, C.-S. Zha, K. D. Litasov, H.-K. Mao, and A. F. Goncharov, *Nat. Commun.* **4**, 2446 (2013).
- [41] N. J. Hartley, S. Brown, T. E. Cowan, E. Cunningham, T. Döppner, R. W. Falcone, L. B. Fletcher, S. Frydrych, E. Galtier, E. J. Gamboa, A. Laso Garcia, D. O. Gericke, S. H. Glenzer, E. Granados, P. A. Heimann, H. J. Lee, M. J. MacDonald, A. J. MacKinnon, E. E. McBride, I. Nam, P. Neumayer, A. Pak, A. Pelka, I. Prencipe, A. Ravasio, M. Rödel, K. Rohatsch, A. M. Saunders, M. Schölmerich, M. Schörner, A. K. Schuster, P. Sun, T. van Driel, J. Vorberger, and D. Kraus, *Sci. Rep.* **9**, 4196 (2019).
- [42] B. L. Holian, M. Mareschal, and R. Ravelo, *J. Chem. Phys.* **133**, 114502 (2010).
- [43] T. H. Cormen, C. E. Leiserson, R. L. Rivest, and C. Stein, *Introduction to Algorithms* (MIT Press, Cambridge, MA, 2009).